by E. P. Stoll

# Picture processing and three-dimensional visualization of data from scanning tunneling and atomic force microscopy

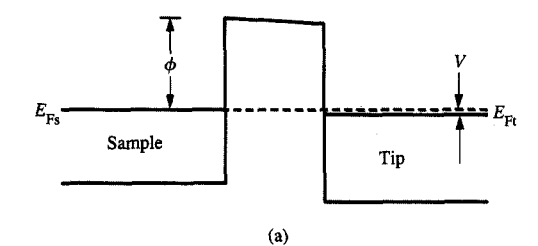
We present an overview of the current status of picture processing and three-dimensional visualization of data from scanning tunneling microscopy and related techniques. The topics we cover include the physical basis of the resolution limit and noise sources in scanning microscopes, the design of restoration filters, and methods of visualizing surface contours and other surface properties by use of shadowing, contour lines, and superimposed colors. Postprocessed images of gold, graphite, biological molecules, the active zone of a laser diode, and silicon illustrate the outstanding quality of these methods.

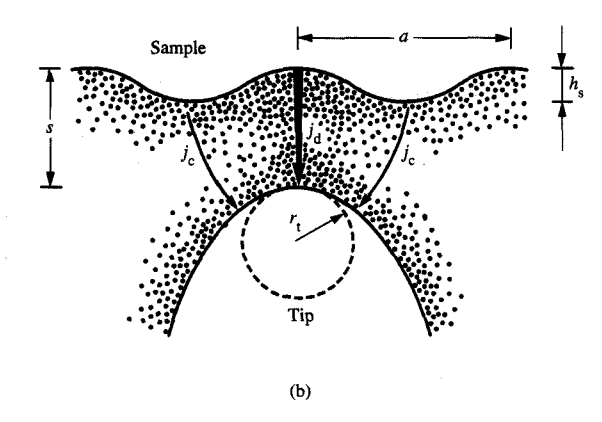
### 1. Introduction

Picture processing in scanning tunneling microscopy and related disciplines [1] entails manipulating raw data to

obtain as much meaningful information as possible [2]. Visualization, on the other hand, is a means of representing the processed data on graphics devices in an informative, aesthetically pleasing, and convincing manner. To this end, it is essential that we understand how data are created and distorted during the acquisition process. Therefore, a short sketch of the underlying physical processes is given. To facilitate understanding for nonspecialists, heuristic arguments rather than rigorous quantum-mechanical derivations are used. Section 2 is devoted to the basic principles underlying the operation of the scanning tunneling microscope (STM), its resolution limit [1], and relevant noise sources [3]. In Section 3, the main features of useful filters and their implementations [3] are described. Finally, the results of judicious processing and visualization on a highresolution graphics display are illustrated by selected STM and related pictures obtained at the IBM Zurich Research Laboratory.

<sup>&</sup>lt;sup>6</sup>Copyright 1991 by International Business Machines Corporation. Copying in printed form for private use is permitted without payment of royalty provided that (1) each reproduction is done without alteration and (2) the *Journal* reference and IBM copyright notice are included on the first page. The title and abstract, but no other portions, of this paper may be copied or distributed royalty free without further permission by computer-based and other information-service systems. Permission to republish any other portion of this paper must be obtained from the Editor.





Schematic diagrams of (a) the potential "felt" by an electron tunneling between two electrodes separated by a tunnel barrier in the free-electron model and (b) the electron density and current flows between a corrugated surface and the probing tip. A net tunneling current arises from electrons with energies between  $E_{\rm Fs}$ , the Fermi level of the sample, and  $E_{\rm Ft}$  that of the tip. V is the tunneling voltage and  $\phi$  the work function of the sample. The currents  $j_{\rm c}$  from adjacent protrusions are much more attenuated than the direct currents  $j_{\rm d}$  due to a larger effective distance s in Equation (1). Their relative contribution is greater when the tip faces a valley of the sample and less when the tip faces a hill.  $r_{\rm t}$  is the radius of curvature of the tip at its apex, s the tip-to-sample distance,  $h_{\rm s}$  the sample corrugation amplitude, and a the lateral distance between two hills or two valleys on the sample.

# 2. Principles of scanning tunneling and related microscopes

The operation of the STM [1] is based on general quantum-mechanical properties of electrons in conducting solids. These particles propagate in the conductor, but form a "cloud" which extends beyond the surface and penetrates into vacuum exponentially with a decay length of  $1/2\kappa_0$ ;  $\kappa_0 = \sqrt{(2m_e/\hbar^2)}\phi$ , where  $m_e$  is the electron mass and  $\phi$  is the average "barrier height" above the Fermi level  $E_{\rm F}$ , the highest energy state occupied by the electrons [see Figure 1(a)]. This leads to a small but nonnegligible overlap of the electron clouds between two conducting electrodes, which are separated

by a small distance s of a few atomic diameters. Applying a small voltage V of the order of a few millivolts between the electrodes gives rise to a tunneling current j of the order of nanoamperes. The very high sensitivity of this quantity to the distance s, arising from the last factor in the expression for the tunneling current [4],

$$j = \frac{e^2}{\hbar} \frac{\kappa_0}{4\pi^2 s} V A_{\text{eff}} \exp\left(-2\kappa_0 s\right) \tag{1}$$

(where  $\hbar$  is Planck's constant, e the electron charge, and  $A_{\rm eff}$  the effective area through which the tunneling current flows), is the reason for the remarkable perpendicular resolution of the STM [1]—of the order of 1% of one atomic diameter. Although this expression has been derived for a simplified model in which both electrodes are represented by flat free-electron-like metals, the above-mentioned crucial factor is present irrespective of the exact properties of the electrodes. Thus, by recording the change in s as the probing tip electrode is scanned parallel to the sample surface while s is kept constant, an image of the surface profile can be recorded.

With heuristic arguments the lateral resolution can be derived from (1) by using a similar simplification: The sample is idealized as a simple metal, in which electrons can move freely. At the sample surface, the potential acting on each electron jumps to the average work function  $\phi$  above the Fermi energy  $E_{\rm F}$  of the electrons, as illustrated in Figure 1(a). If the corrugation of the sample surface [see Figure 1(b)] is very shallow and extended, i.e., if the period a is much larger than the tip radius  $r_i$ , s, or  $1/2\kappa_0$ , the apparent corrugation amplitude  $\Delta s$  of the surface, which is traced by the tip at constant total tunneling current j and is accessible in real experiments, faithfully reproduces the sample surface profile ( $\Delta s = h_s$ ); i.e., there is no blurring. However, if the corrugation of the sample surface is deep, so that a is comparable to s and  $h_s$ , the electron density tends to become more uniform away from the surface, and  $\Delta s$  becomes noticeably smaller than  $h_{\epsilon}$  when s is increased. An intuitive explanation for this phenomenon is that if the tip is facing a depression, the electron density has components from the elevated regions nearby, thus increasing the local tunneling current. Furthermore, the above-mentioned smoothing of the electron density over a larger area diminishes the current if the tip faces an elevation. Both effects together decrease the difference of the perpendicular tip positions corresponding to a preset constant current at "hills" and "valleys." A further reduction of the lateral resolution is due to the finite size of the tip; what becomes important is the radius of curvature r, at its apex. These contributions are contained in the formula

$$\frac{\Delta s}{h_{\rm s}} = \exp\left[-\frac{\pi^2(r_{\rm t} + s)}{\kappa_0 a^2}\right],\tag{2}$$

which takes into account the fundamental Fourier component of the sample corrugation [5, 6].

For picture-processing purposes, the Fourier transform of Equation (2),

$$\frac{\Delta s(q)}{h_{\rm c}(q)} = \exp\left[-\frac{q^2(r_{\rm t}+s)}{4\kappa_0}\right],\tag{3}$$

where the coordinate q corresponds to  $2\pi/a$ , is more convenient. Moreover, it has more general validity.

The derivation of Equations (2) and (3), based on rather restricted simplifications, is valid only for typical simple metal surfaces such as aluminum, silver, or gold. For transition-metal, semimetal, and semiconductor samples, deviations are expected, as shown in [7]. In view of this, Equation (3) must be considered merely as a guide for a general picture-processing algorithm containing the essential feature that Fourier components with large q decrease rapidly with increasing s. Quantitative restoration and interpretation of STM data require extensive numeric calculations on supercomputers, taking into account detailed properties of sample and tip as well as, at short distances, their mutual interactions.

Similar considerations apply to an even larger extent to the restoration and interpretation of scanning tunneling spectroscopy (STS) [8] data, which are recorded by varying the tunneling voltage V over a range of several volts, or for atomic force microscopy (AFM) [9] data, where the force, or force derivative, between tip and sample is measured. In both cases contributions with shorter or longer decay lengths appear in addition to the main exponential decay apparent in Equation (1) of the recorded signal [4, 10], and the resolution function (3) must be assumed to be only a guide for overall features.

As a consequence, and because they can only be estimated in a very indirect way, introducing specific values for the parameters s,  $r_t$ , and  $\kappa_0$  in Equation (3) is not worthwhile. For picture-resolution and data-interpretation purposes, it is much more convenient to rewrite Equation (3) as

$$\frac{\Delta s(q)}{h_s(q)} = \exp\left(-\frac{q^2}{q_0^2}\right),\tag{4}$$

where  $q_0$  becomes a picture-processing parameter limited to a physically reasonable range [11].

The most important sources of noise affecting STM and related microscopy data are schematically illustrated in Figure 2 [12]. The noise from mechanical vibrations penetrating into the suspension system [13] is usually much less than the other noise contributions under very adverse environmental conditions. Due to the enormous number of electrons contributing to the tunneling current at the nanoampere level, the shot noise is negligible

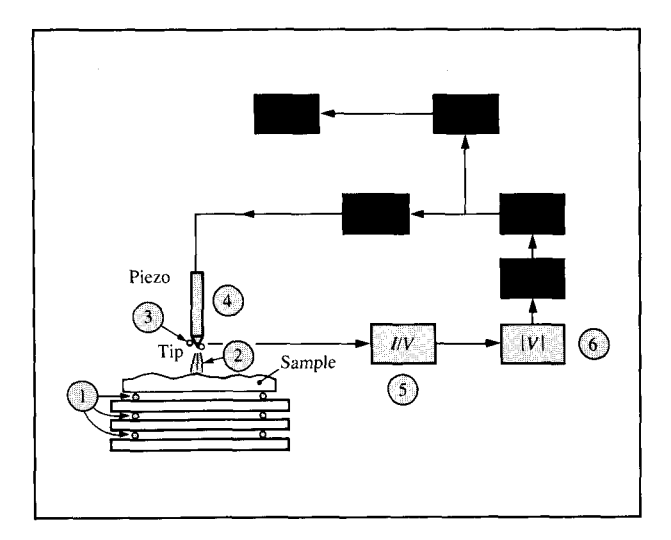
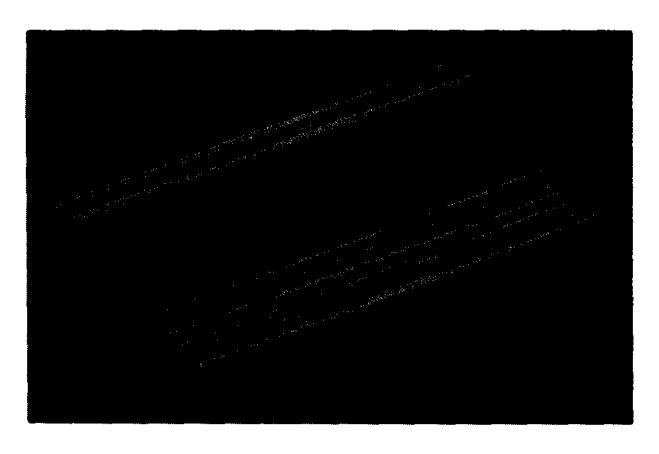


### Figure 2

Schematic diagram of the STM control electronics and suspension system. Noise sources: (1) the nonideal suspension system [13], through which environmental vibrations penetrate; (2) white shot noise accompanying the small tunneling current of 1 nA, i.e., 1010 elementary charges per second; 1/f-like noise due to (3) host or foreign atoms jumping on the tip or the sample; (4) time-dependent aftereffects in the piezoceramic scanning actuators [14]; (5) resistor and semiconductor noise in the operation amplifier (I/V-converter); (6) high-frequency noise in the rectifier (IVI) (J. Schmid, IBM Research Division, Rüschlikon, Switzerland, 1989; private communication). In the I/V-converter, white Johnson noise which may be significant at high frequencies is also generated [15]. Other electronic elements such as the nonlinear device generating the signal logarithm (Log), the integrating control unit (ICU), the high-voltage amplifier (HVA), and the analogdigital converter (ADC) which transmit the tip height position signal in digital form to the microprocessor (µP) contribute much less to the 1/f noise.

against 1/f-like noise. The much more severe Johnson noise of the I/V converter also contributes only at high frequencies [15]. This behavior is completely different from that of electron microscopes, where the shot noise of the high-energy electrons constitutes the largest contribution. Therefore, noise filters must satisfy different requirements than in standard electron microscopy.

To estimate the effects of noise, the tip displacement signal was recorded as a function of time at a fixed position and displayed like an STM image, i.e., with x and y appearing as displacements corresponding to the scanning motion in a typical measurement. The striking features in the noise image of Figure 3 are extended stripes parallel to the fast x "scan" direction, exhibiting small modulations which reflect very slow movements of the tip perpendicular to the sample with periods longer than 30 seconds. As is shown later, such stripes are visible in nearly every real STM picture.



Time-dependent height position of a tungsten tip above a graphite sample at 60 K with an applied voltage of 30 mV leading to a current of 60 nA [3]. The picture was generated by plotting this position from left to right for 1.5 seconds, waiting another 1.5 seconds, then plotting the second line, etc. as in a real STM image. For better contrast the picture was rotated 30° counterclockwise prior to shadowing. Blue denotes the minima and red-brown the maxima of the picture, which resemble lakes and hills on a map. The height variations along the slow-scan direction are due to low-frequency 1/f-like noise components.

It is readily apparent that such a slow unintentional tip motion produces misleading artifacts in the background of STM images, which make it difficult to interpret physically significant nonperiodic structures at an angle with the fast-scan direction without some a priori knowledge. As a warning for uncritical STM users, it should be emphasized that 1/f noise is strongly correlated and can generate appealing self-similar landscapes [16]. To account for the important information from this experiment in picture-processing procedures, the noise image was fitted with a  $(1/f)^{\beta}$  rule, yielding  $\beta = 1.4 \pm 0.2$  [3].

Here, the difference from the 1/f noise interpretation of [17] should be clarified. Those authors claim that 1/f noise should only be included parallel to the fast-scan direction, because in the perpendicular direction they recognized only white noise over relatively small, rapidly scanned areas. A partial explanation for this (at first sight) paradoxical observation may be that the 1/f noise remaining in the y-direction after averaging over each x-scan is still large and difficult to distinguish from white noise. On the other hand, a large noise component requires that the Fourier coefficients corresponding to  $q_x = 0$  must be suppressed in the filtering procedure. Therefore, in the end, the difference between our procedures and theirs [17] is rather small for very noisy pictures.

# 3. Sampling and filtering

Data from STM and other scanning microscopies are usually sampled with an increment  $\Delta x$  parallel to the scans, and are thus digitized. While the tip is moved back for the next recording, it is moved perpendicular to the scan direction and parallel to the surface by another increment  $\Delta y$ ;  $\Delta x$  and  $\Delta y$  must be chosen small enough to satisfy the Whitaker-Kotelnikov-Shannon sampling theorem [18]. This is achieved if these increments are smaller than the half-point spread due to the finite lateral resolution of the instrument. Therefore, care must be taken that with improved instrumental resolution  $\Delta x$  and  $\Delta y$  are also reduced accordingly. Otherwise, aliasing artifacts can be expected (see [11] for details).

The primary task of image filters is to remove picture blurring due to the finite resolution and to suppress noise in order to obtain a smoothed picture that still retains physically relevant information. The blurring while the data are recorded amounts to a convolution, which in principle can be eliminated by the inverse process, the deconvolution. In practice, however, this is difficult and unreliable unless the main noise contributions are properly treated.

A further important property inherent in all filters is that noise can never be suppressed without also destroying some significant information. Therefore, good filters must be able to separate those parts of the picture where the information component of the signal is much larger than the noise contribution from those parts where the noise is stronger. When this is the case, the noisiest parts can often be identified and set equal to a constant or a smooth background. In most cases, signal and noise are nearly equally distributed over the entire picture. Therefore, the picture must be filtered according to other properties. A linear superposition of slow- and fastchanging picture elements g(x, y) can be handled via the Fourier transform, which is powerful enough for a wide variety of cases. Then the filtering is made in Fourier space, and the filtered image is transformed back into real space. To avoid artifacts due to undesired mappings of sharp boundary edges into the interior of the restored picture, a periodic contribution with soft picture borders must be forced prior to the first Fourier transform.

For the sake of simplicity, we now assume that the resolution point spread function (PSF) h(x, y) and the noise n(x, y) are independent of the "true" picture f(x, y). This leads to the linear convolution relation

g(x, y)

$$= \int dx'dy' f(x - x', y - y') h(x', y') + n(x, y), \quad (5)$$

which is conveniently transformed into Fourier space,

$$G(\hat{q}) = F(\hat{q})H(\hat{q}) + N(\hat{q}), \tag{6}$$

where capitals denote the Fourier-transformed functions. In principle, this equation can formally be solved for  $F(\hat{q})$ ,

$$F(\hat{q}) = G(\hat{q})/H(\hat{q}) - N(\hat{q})/H(\hat{q}), \tag{7}$$

but the second term should contain full information not only about the amplitude but also about the *phase* of the noise  $N(\hat{q})$ . Since the latter information is not available, the second term in Equation (7) cannot be directly estimated. Furthermore, the noncompensated noise in  $G(\hat{q})$  is amplified by division by  $H(\hat{q})$  at large wavenumbers q where the PSF is small. This property holds for all deconvolution procedures, and everyone is warned to not use procedures such as those advocated for example in [19] without properly treating the noise.

To minimize the deviation between the surface profile and the reconstructed picture, an algorithm based on the notion of Wiener filters [11, 20] has been implemented. Because the noise does not allow the profile to be restored even if the PSF is known precisely, a filter procedure which is easily applicable to all STM pictures evaluates the best least-squares estimate,

$$F_{\circ}(\hat{q}) = W(\hat{q})G(\hat{q}), \tag{8}$$

where the filter function

$$W(\hat{q}) = \frac{H^*(\hat{q})}{|H(\hat{q})|^2 + \phi(\hat{q})} \tag{9}$$

depends on the resolution PSF  $H(\hat{q})$  (the asterisk denotes complex conjugation) as well as on the estimated noise-to-signal power ratio  $\phi(\hat{q}) = |N(\hat{q})/[F(\hat{q})H(\hat{q})]|^2$ . As expected for  $N(\hat{q}) = 0$ ,  $\phi(\hat{q})$  vanishes, and Equations (8) and (9) together reduce to Equation (7).

As mentioned in Section 2, STM data are affected mainly by 1/f noise; at high frequencies, white Johnson noise from the digitized rectifier sampling may also contribute. As described in the caption of Figure 3, the tip motion transforms the time-dependent noise  $\tilde{n}(t)$  into an anisotropic space-dependent noise function [2]

$$n(x, y) = \tilde{n} \left( \frac{x + 2L_x \Delta x y / \Delta y}{c} \right), \tag{10}$$

with  $\Delta x$  and  $\Delta y$  defined as at the beginning of this section;  $L_x$  is the number of sampled points in one x-scan record, and c is the scanning speed. The corresponding discrete Fourier transform is therefore

$$N(\hat{q}) = \tilde{N} \left\{ c \left[ q_x^2 + \left( \frac{q_y}{2L_x \Delta x / \Delta y} \right)^2 \right]^{1/2} \right\}, \tag{11}$$

where  $q_x = j[2\pi/(L_x \Delta x)]$  and  $q_y = k[2\pi/(L_y \Delta y)]$ ; j and k are integer numbers, and  $L_y$  is the number of scans in the

STM picture. It is clear from Equation (11) and from the remarks at the end of Section 2 that the effect of the 1/f-like noise is much more pronounced in the y-direction than in the x-direction. As a matter of fact, the  $(q_x = 0, q_y)$  Fourier components contain the strongest 1/f-like noise contamination, whereas those with  $q_x \neq 0$  contain mostly physically relevant picture information and are only slightly distorted by white and high-frequency rectifier sampling noise. By using the noise measurement described in Section 2 and [3], the amplitude of the noise-to-signal function

$$\phi_{\beta}(\hat{q}) = \frac{\alpha}{\left[ (2L_{y}j)^{2} + k^{2} \right]^{\beta/2}},$$
(12)

with  $\beta=1.4\pm0.2$  [3] can be determined. If useful information is itself obscured by Fourier noise components with small  $|q_y|$  values, this assumed noise amplitude may be too strong; to obtain reasonable results, we found it advantageous to let  $\alpha$  approach  $L_y$  asymptotically.

For large j,  $\phi_{\beta}(\hat{q})$  as defined in Equation (12) becomes smaller than the Johnson noise [15] and the high-frequency rectifier sampling white-noise estimate  $\phi_0$ , so that the deviation between  $F_{\rm e}(\hat{q})$  and  $F(\hat{q})$  would become larger than  $|F(\hat{q})|$ . Such large deviations produce ugly artifacts which can be avoided by *robust filtering* [21], so that the deviations do not anywhere become larger than the picture information. Accordingly, we therefore take

$$\phi(\hat{q}) = \begin{cases} \phi_{\beta}(\hat{q}), & \text{if } \phi_{\beta}(\hat{q}) > \phi_{0}, \\ \phi_{0} & \text{otherwise.} \end{cases}$$
 (13)

Special care must be taken when the signal g(x, y) is the derivative against the scan direction x [15] and must be integrated. Because integration corresponds to a division through  $q_x$  in Fourier space, the  $1/f^\beta$  noise is transformed into  $(1/f)^{2+\beta}$  noise and can afterwards no longer be eliminated according to Equations (12) and (13). Therefore, for  $q_x = 0$ ,  $F_e(\hat{q})$  must be set to 0, and for  $q_x \neq 0$ ,

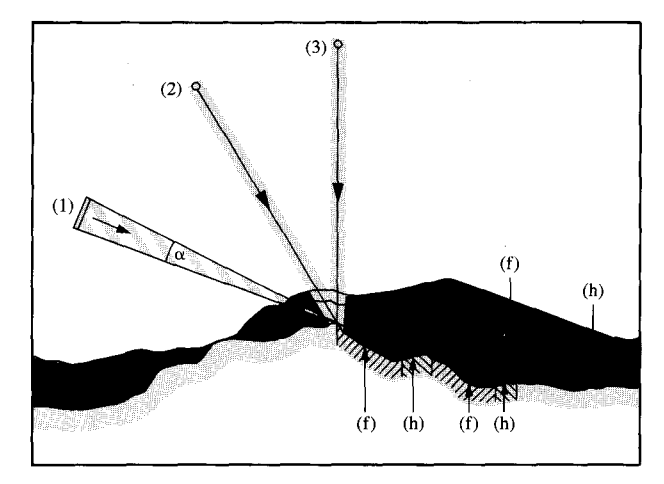
$$F_{\sigma}(\hat{q}) = W(\hat{q})G(\hat{q})/q_{x}, \tag{14}$$

with

$$\phi_{\beta}(\dot{q}) = \frac{\alpha}{\left[ (2L_{\nu}j)^2 + k^2 \right]^{\beta/2} \tan^{-1}(j^2/j_2)},\tag{15}$$

where  $j_2$  is the normalized second moment of a roughly estimated picture function  $F_e(\hat{q})$ , divided by  $2\pi/(L_x\Delta x)$ . The tan<sup>-1</sup> function is chosen because of its proper limiting behavior for small values of  $|q_x|$  and its

<sup>&</sup>lt;sup>1</sup> J. Schmid, "The Electronics of the STM Control Unit," IBM Research Division, Rüschlikon, Switzerland, 1989 (private communication).



Schematic illustration of simulated illumination, shadowing, and line and area hiding. Source (1) with an incident angle of  $24^{\circ}$  is rod-like, producing half-shade (h) and full-shade (f). Its projection angle  $\alpha$  is  $6^{\circ}$ . To display the information in the shadow regions, point-like sources (2) and (3) with inclination angles of  $60^{\circ}$  and  $90^{\circ}$  and intensities equal to half that of source (1) are assumed. After the picture is tilted about the x-axis, the top line and visible area (a) are drawn first. The pixels in that area can be overwritten by those of the next line (b). Then, by successively processing one line and its corresponding area after another, the entire picture is completed.

saturation for values larger than the square root of the normalized second moment.

# 4. Three-dimensional surface visualization

Once the surface profile has been restored, it must be displayed in such a way that its three-dimensional appearance can be visualized. In a first step, different height levels are characterized by a false-color or graytone code and can be quantified with contour lines. On the other hand, the corrugation of the profile may be represented by shading under simulated illumination, the reflectivity being maximum at perpendicular incidence of light and zero at grazing incidence. The structural rendition is enhanced by simulating shadows. Experience in photography indicates that optimum shading can be achieved only if objects are illuminated from different judiciously placed sources. As a counterexample, nearly everyone remembers pictures of the moon where the shadow regions are so dark that all information in those regions is hidden; this is because sunlight, since it is not scattered by air and dust as on earth, illuminates the moon as a single source. To prevent such "moonscape"like pictures, shading is simulated with three light sources, as illustrated in Figure 4. Sharp shadow boundaries are softened by a light source extended in at least one direction, thus producing half-shade. Together

with shadowing intensities to characterize the surface profile, color information may also be used to display other local physical quantities recorded simultaneously, such as the conductance spectrum [8], the barrier height [22], the electrical potential produced by another current along the sample [23], and the force components acting on the tip or their gradients [9].

To visualize scientifically relevant information, two kinds of graphic display modes are used: top views, which preserve the correct picture aspect ratio, and parallel projections obtained by rotating the picture coordinates about the x-axis. Such parallel projections have the advantage of minimizing the very time-consuming determination of hidden lines (see Figure 4) and of preserving correct distances in the x-direction. Similar simplification is achieved by locating the simulated light sources in one common perpendicular incident plane parallel to the x-direction. Each picture element (pel or pixel) line along the x-scan can then be treated independently of the others.<sup>2</sup>

We know from the physiology of the eye and the brain that humans can distinguish of the order of 10° to 10° different levels of light intensity, color, or saturation. Very sophisticated graphics stations use 24 bits (or 3 bytes) per pixel (one byte for each fundamental color) to produce high-quality pictures without visible color quantization steps. Simpler workstations, such as those available in most physics laboratories, are able to display simultaneously a much smaller set of hues chosen from a lookup table. If, for example, one byte, i.e., 256 different values, can be assigned to each pixel, only 16 different intensities can be combined with 16 different colors. To avoid the resulting ugly quantization artifacts, an optimum dot pattern threshold matrix interpolation scheme [24] is applied to adjacent  $4 \times 4$ -pixel arrays for intensities and colors. This kind of interpolation algorithm has the advantage of removing the degradation of spatial resolution that can occur when picture properties change considerably between neighboring pixels. The well-known disadvantage of this procedure, namely that it produces aliasing patterns due to dot size overlap, is reduced on graphic displays, because only dots of different intensities but of nearly the same size are exchanged.

# 5. Illustrative examples of postprocessing

To demonstrate the filtering and visualization capability and suitability of our procedures, examples of postprocessed STM and related data are shown. Raw scans and a processed picture of a gold (100) single-crystal surface sample [25] are displayed first because of the relative simplicity of its electronic structure.

<sup>&</sup>lt;sup>2</sup> R. F. Voss, "Enhanced Surface Displays," IBM Research Division, Yorktown Heights, NY, 1989 (private communication).



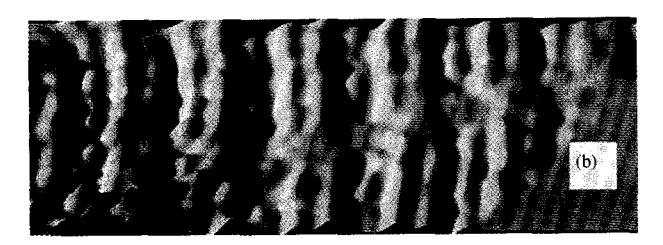


### Figure :

STM picture of a gold (100) surface measured at room temperature with a tunneling voltage of 40 mV in a vacuum of  $10^{-8}$  Pa. The improvement in the postprocessed picture (b) compared to the raw scan data (a) is striking. Irregular spacings between scan lines due to 1/f noise are marked with bars in (a). The filter parameters  $q_0$  and  $\phi_0$  were chosen such that the surface appeared smooth and the overall features did not depend on a relative variation of these parameters of the order of two. To give a better rendition of a gold surface, the intensities of the second and third light sources were reduced to a factor of 0.4 and 0.1 of those of the first source, and the lookup table simulated golden colors. The extension of (b) is  $7.5 \times 8.5$  nm, and the tilting angle about the x-axis is  $50^{\circ}$ . The other picture-processing parameters correspond to those of Figure 4.

The following characteristic features of the extended pattern apparent in the postprocessed image in Figure 5(b) can readily be recognized: (1) the changeover from single (or triplet) ridge maximum and single minimum on the left-hand side to double maximum and double minimum on the right-hand side; (2) the relatively flat diagonal stripe extending from the left bottom to the right top corner. These features are due to spatial interference in the positions of surface atoms, and form a distorted triangular top layer and the square layers below [25]. Figure 5(a) shows the irregularities in the separations between scan lines after the third line and below the first third of the scanned area from the top, marked with bright bars, which are due to 1/f noise and are nearly always visible in raw STM data.

Figure 6 shows the much simpler  $(1 \times 2)$  reconstruction on terraces of a vicinal gold (110) surface, one of the first imaged with STM [26]. Instead of the tip position z(x, y), the derivative  $\partial j(x, y)/\partial x$  was recorded



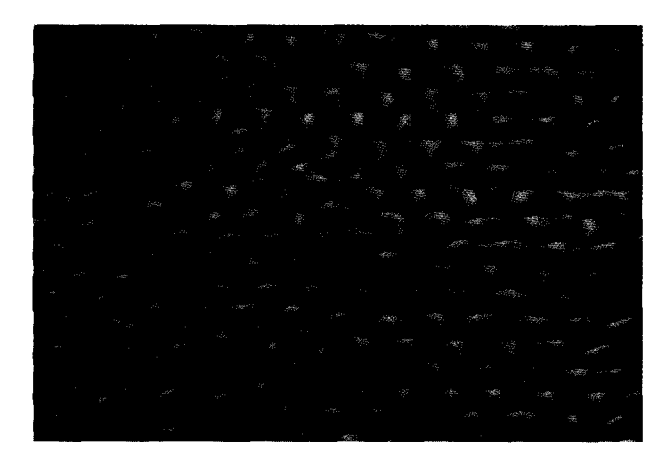


### Figure 6

Plot of integrated  $\partial j/\partial x$  data of a vicinal gold (110) surface exhibiting (1 × 2)-reconstructed terraces and an extension of 50 × 50 nm (a) without and (b) after 1/f-noise filtering [Equation (15)]. The ripples in (a) due to 1/f noise are marked with bars. Values of 0.004 scan length and 0.02 are used for the filter parameter  $1/2q_0$  and  $\phi_0$ . The other picture-processing parameters correspond to those of Figure 5.

in an experiment<sup>3</sup> recently proposed [15] as a method for reducing various forms of noise. In contradiction to the authors, we claim that application of their formula to restore the conventional topography z(x, y) leads to spurious ridges marked by bright bars parallel to the scan direction due to 1/f noise, as seen in Figure 6(a). Deviations from the exponential function in Equation (1) due to image forces [22] as well as to other nonlinearities in the feedback loop (Figure 2) couple the current 1/f noise with the recorded  $\partial j/\partial x$  signal. This rather small noise is then considerably amplified due to the required integration [Equation (14)]. Our filter procedure [Equation (15)] removes this noise, as demonstrated in Figure 6(b). The ripples vanish almost entirely and the

<sup>&</sup>lt;sup>3</sup> J. K. Gimzewski and R. R. Schlittler, "Differential Scanning Tunneling Microscopy of Au (110) (1 × 2) Reconstructed Surfaces," IBM Research Division, Rüschlikon, Switzerland, 1989 (unpublished work).



Topographic image of cleaved pyrolytic graphite at 6.8 K in vacuum with a tunneling voltage of 20 mV and a tunneling current of 7.5 nA [12]. The filter parameters were  $1/2q_0=1/3$  of the surface lattice constant a=0.28 nm and  $\phi_0=0.02$ . The lookup table was designed to simulate the colors of a landscape, as in Figure 3. The plotted area is a square with an extension of  $3.3\times3.3$  nm and a tilting angle of 50° about the x-axis. The other picture-processing parameters are those of Figure 4. Unit cells showing all six carbon atoms in the hexagonal ring are marked with an x.

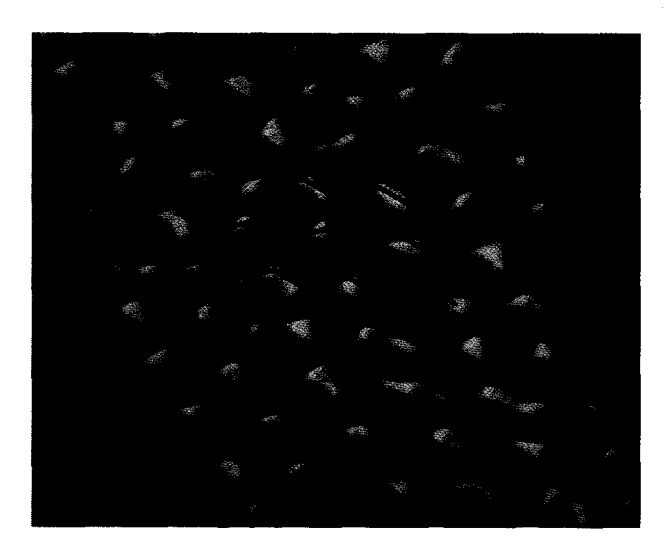


# Figure 8

Topographic image of graphite measured with an AFM at room temperature and ambient pressure [32] on a rhomboid with horizontal and oblique extensions of 1.5 and 2.5 nm. The filter parameters  $q_0$  and  $\phi_0$  were chosen such that the surface appeared smooth and the overall features did not depend on a relative variation of the order of two. The other picture-processing parameters correspond to those of Figure 7. The hexagonal net is a guide to assist the eye in recognizing the carbon hexagons.

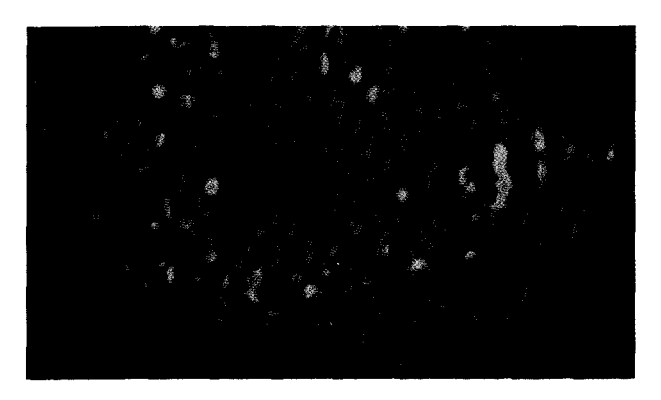
atomic rows characteristic of the  $(1 \times 2)$  reconstruction become clearly visible. Therefore, the proposal in [15] is

misleading in suggesting that data postprocessing is not required with this method.

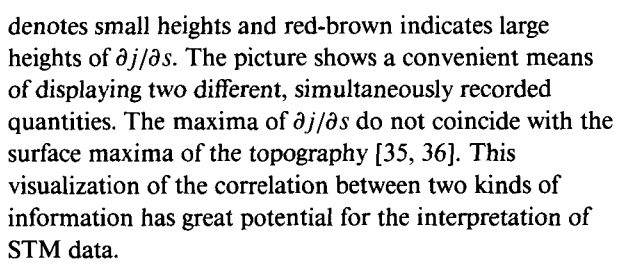
One important advantage of STM is that it can be applied to *nonperiodic* surfaces or to situations in which deviations from periodicity are important. In the first low-temperature measurement on a cleaved graphite sample [12], such a break in periodicity was apparent, as shown in Figure 7. Due to the special electronic structure of graphite [27-29], the STM does not merely measure the atomic corrugation, and the resolution PSF does not satisfy Equations (2) and (3). Nevertheless, Fourier amplitudes with large  $|\hat{q}|$  values cannot contribute to the picture information as proposed in [7]. Therefore, filtering with Equation (4), where  $1/2q_0$  is set to one-third of the hexagonal lattice constant, produces a contrasted picture without suppressing important information. A further problem occurs in the generation of highresolution images of graphite with tips covered with small graphite single-crystal flakes [30, 31]. Because of their similar structure, such tips produce complex moiré patterns [31]. It is rather difficult to design filters able to deconvolute such artifacts; the process would have to be performed iteratively.

For comparison of the preceding postprocessed STM picture with one obtained with an atomic force microscope, Figure 8 shows one of the first surfaces for which atomic resolution was achieved with an AFM [32]. The corrugation, of the order of 1/70 of the surface lattice constant, is very small. As in the STM picture, approximately only every second carbon atom appears as a maximum. Sometimes, when the average hexagonal net is used as a guide, all six carbon atoms in the characteristic hexagonal rings of graphite are recognizable. The changeover from a full hexagonal arrangement to a trigonal one can be explained by a graphite flake attached to the probing tip [33], as in the case of STM [30, 31].

The total electron density of cleaved graphite is expected to show very little corrugation. This is confirmed by STM images recorded at sufficiently large tunneling voltages (>1 V); the observed corrugation becomes negligible over wide areas [27, 34]. Therefore, graphite was proposed as an ideal support for organic and biological samples. Unfortunately, most molecules stick to it very poorly and are trapped only at surface steps. Figure 9 shows a filament of uncoated air-dried doublestranded DNA [35]. Contour lines are added to help highlight the strand structure. In a shaded plot like this one, it is important to select suitable intensity levels of the contour lines so that they are visible but do not distort the impression created by shading. The color code, on the other hand, indicates the local barrier height, which in turn reflects local electric dipole moments due to charged chemical groups [22]. Blue

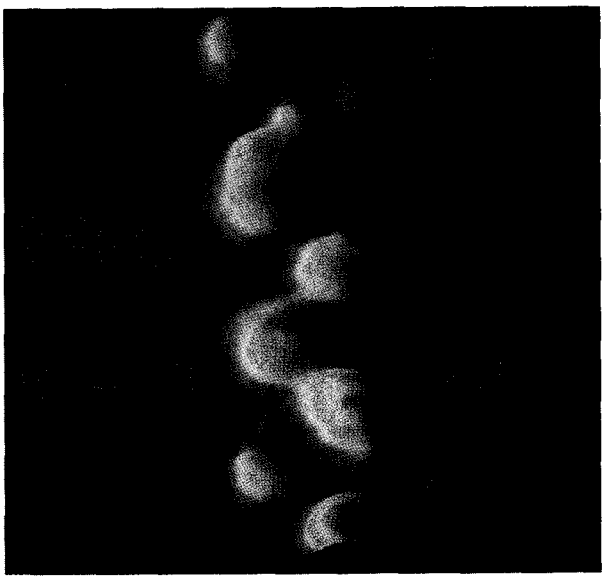


STM topographic image (shading) combined with a color-coded  $\partial j/\partial s$  image on an area of 65  $\times$  40 nm. To enhance the impression of the topography, contour lines with lower intensities have also been added. The spacing between these lines corresponds to 0.1 nm. (In the color code, blue denotes small and red-brown large values of  $\partial j/\partial s$ .) The other picture-processing parameters correspond to those of Figure 8. The graphite substrate inside the ring is lower by an amount corresponding to a graphite double layer. This is made visible in the scan shown in [35]: The DNA filament is trapped on the resulting step.



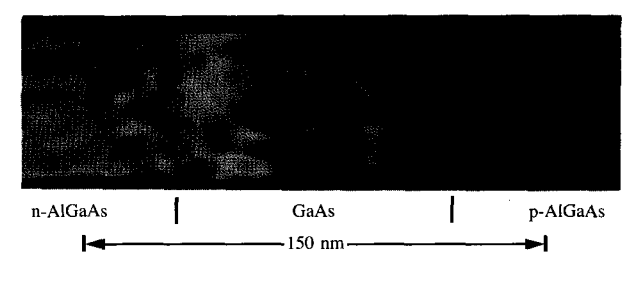
Because it is quite difficult to attach organic molecules to a bare graphite support, as was done with standard electron microscopy in the first detailed STM examination of large macromolecules, namely the DNA-recA protein complex [35, 36], the organic molecules were coated with a thin Pt-C film. A postprocessed image of a portion of the originally observed scans [35] in Figure 10 exhibits the structure consisting of single recA monomers wound in a spiral around a DNA chain.

Figure 11 displays the topography and the electrical potential drop along the cleaved surface of a forward-biased GaAs/AlGaAs double-heterojunction (DH) laser diode [37]. In this case, the color code exhibits the drastic waterfall-like potential drop at the interfaces despite the rather shallow topography. The red-brown and blue spots indicate local maxima and minima of the potential superimposed on the monotonic decrease of the external potential applied across the diode. The structure parallel to the junction interfaces may reflect local space-charge variations due to inhomogeneities of the doping profile.



### Figure 10

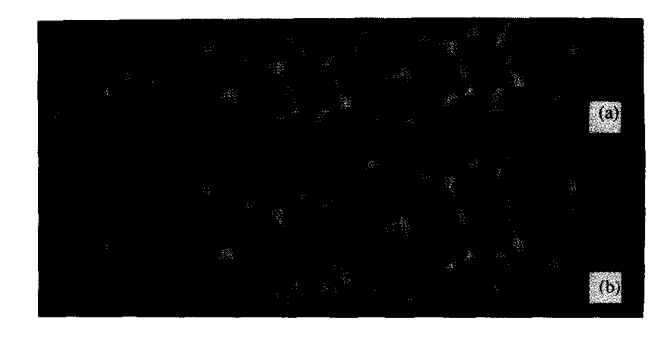
STM image of a metal-coated, freeze-dried DNA-recA filament cluster. From the scans in [35], only the part containing the recA proteins was processed; its extension is  $50\times45$  nm, and the picture-processing parameters correspond to those of Figure 8.



### Figure i

Combined topographic (shading) and potentiometric (colors) image of a flat part of a cleaved double-heterojunction structure [37]. In the color code, red-brown denotes high and blue low electric potential. The incidence angle of the first source is 15° to produce more contrast on the rather shallow topography. The other picture-processing parameters correspond to those of Figure 8.

Our last picture, Figure 12, shows a combination of the surface topography (shading and contour lines) and tunneling spectroscopy (colors) originally recorded on a narrow stripe of a reconstructed (111)  $7 \times 7$  silicon surface [1]. Although the general correspondence between maxima in the topography and minima in the spectroscopy is apparent, it merely represents a background effect without new physical content [1]. The dominant true spectroscopic features in the voltage range



Combined topographic (shading) and spectroscopic (colors) image of the reconstructed (111)  $7 \times 7$  silicon surface, taken with a tip at -1.0 V [1]: (a) tilted 50° and (b) top view. The distance between the lowest minima surrounded by the maximum hexagon is 2.7 nm. To enhance the impression of the topography, contour lines with lower intensities are drawn in (b). The spacing between these lines is of the order of 0.05 nm. In the color code, blue denotes small and red-brown large values of  $\partial j/\partial V$ . The dominant true spectroscopic maxima due to dangling bonds on the "rest atoms" in the lower half of the surface unit cell are marked  $\uparrow$ . The other picture-processing parameters correspond to those of Figure 8.

of the measurement are the three pronounced maxima marked  $\uparrow$ , which correspond to tunneling out of occupied dangling-bond states, as confirmed later in more extensive measurements [38]. Adequate image processing will allow the rich information contained in this first spectroscopic picture of (111)  $7 \times 7$  silicon to be visualized in one single picture.

### 6. Concluding remarks

Data from scanning tunneling microscopy and related techniques are impaired by various noise sources and by a nonideal and incompletely known resolution function. The most troublesome 1/f-like noise can be removed by postprocessing with Wiener-type filters. The same kind of filter also reduces the influence of other kinds of noise and deconvolutes the blurring due to finite resolution. When contour lines are added and a suitable color code employed, three-dimensional surface profiles can be visualized by the shadow they cast when exposed to judiciously placed light sources. This enables users to display data on graphics devices in a manner both aesthetically pleasing and informative and convincing. The choice of colors via lookup tables is analogous to the mixing of colors by an artist on his palette; thus the possibilities for aesthetic renditions are virtually unlimited. Using a few selected STM and related microscopy pictures as examples, we have demonstrated the effectiveness of different judiciously chosen representations.

# **Acknowledgment**

All the colleagues who have enhanced our efforts over the past six years with suggestions to improve the processing and visualization of data are gratefully acknowledged. Special thanks go to J. K. Gimzewski and R. R. Schlittler for providing their gold data prior to publication and to A. Baratoff (particularly for proofreading the manuscript), S. Ciraci, A. Moel, Ch. Gerber, D. W. Pohl, J. Schmid, G. Travaglini, and R. F. Voss for helpful discussions.

# References

- G. Binnig and H. Rohrer, "Scanning Tunneling Microscopy," IBM J. Res. Develop. 30, 355 (1986).
- E. Stoll and A. Baratoff, "Restoration and Pictorial Representation of Scanning-Tunneling-Microscope Data," *Ultramicrosc.* 25, 149 (1988).
- E. Stoll and O. Marti, "Restoration of Scanning-Tunneling-Microscope Data Blurred by Limited Resolution, and Hampered by 1/f-Like Noise," Surf. Sci. 181, 222 (1987).
- J. Simmons, "Generalized Formula for the Electric Tunnel Effect Between Similar Electrodes Separated by a Thin Insulating Film," J. Appl. Phys. 34, 1793 (1963).
- E. Stoll, A. Baratoff, A. Selloni, and P. Carnevali, "Current Distribution in the Scanning Vacuum Tunneling Microscope: A Free Electron Model," *J. Phys. C.* 17, 3073 (1984); N. Garcia, C. Ocal, and F. Flores, "Model Theory for Scanning Tunneling Microscopy: Application to Au(110)(1 × 2)," *Phys. Rev. Lett.* 50, 2002 (1983).
- E. Stoll, "Resolution of the Scanning Tunneling Microscope," Surf. Sci. 143, L411 (1984); J. Tersoff and D. R. Hamann, "Theory and Application for the Scanning Tunneling Microscope," Phys. Rev. Lett. 50, 1998 (1983).
- A. Baratoff, "Theory of Scanning Tunneling Microscopy— Methods and Approximations," *Physica* 127B, 143 (1984); J. Tersoff, "Sample-Dependent Resolution in Scanning Tunneling Microscopy," *Phys. Rev. B* 39, 1052 (1989).
- 8. G. Binnig, K. H. Frank, H. Fuchs, N. Garcia, B. Reihl, H. Rohrer, F. Salvan, and A. R. Williams, "Tunneling Spectroscopy and Inverse Photoemission: Image and Field States," *Phys. Rev. Lett.* **55**, 991 (1985).
- 9. G. Binnig, C. F. Quate, and Ch. Gerber, "The Atomic Force Microscope," *Phys. Rev. Lett.* **56**, 930 (1986).
- 10. D. W. Pohl, "Classic and New Trends in Scanning Tunneling Microscopy," presented at the Adriatico Research Conference on Scanning Tunneling Microscopy, July 28-31, 1987 in Trieste; idem, "STM and Related Techniques," Point and Extended Defects in Semiconductors, G. Benedek, A. Cavallini, and W. Schröfer, Eds., Plenum Press, New York, 1989, p. 183.
- E. Stoll, "Information- and Image-Processing of Scanning-Tunneling-Microscope Data," W. F. Fagan, Ed., SPIE—Optics in Engineering Measurements 599, 442 (1985).
- O. Marti, "Scanning Tunneling Microscope at Low Temperatures," Ph.D. Thesis No. 8095, Swiss Federal Institute of Technology, ETH, Zurich (1986).
- Ch. Gerber, G. Binnig, H. Fuchs, O. Marti, and H. Rohrer, "Scanning Tunneling Microscope Combined with a Scanning Electron Microscope," Rev. Sci. Instrum. 57, 221 (1986).
- S. Vieira, "The Behavior and Calibration of Some Piezoelectric Ceramics used in the STM," IBM J. Res. Develop. 30, 553 (1986).
- S. W. Abraham, C. C. Williams, and H. K. Wickramasinghe, "Noise Reduction Technique for Scanning Tunneling Microscopy," Appl. Phys. Lett. 53, 1503 (1988); idem, "Differential Scanning Tunneling Microscopy," J. Microsc. 152, 599 (1988).
- R. F. Voss, "Random Fractals: Characterization and Measurement," Scaling Phenomena in Disordered Systems, R. Pynn and A. Skjeltorp, Eds., Plenum, New York, 1985, p. 1;

- idem, "Random Fractal Forgeries," Fundamental Algorithms for Computer Graphics, R. A. Earnshaw, Ed., NATO ASI Series, Vol. F 17, Springer-Verlag, Berlin, 1985, p. 805.
- 17. Sang-Il Park and C. F. Quate, "Tunneling Microscopy of Graphite in Air," Appl. Phys. Lett. 48, 112 (1986).
- See, e.g., A. Rosenfeld and A. C. Kak, *Digital Picture Processing*, Academic Press, Inc., New York, 1982, second edition.
- R. Chicon, M. Ortuno, and J. Abellan, "An Algorithm for Surface Reconstruction in Scanning Tunneling Microscopy," Surf. Sci. 181, 107 (1987); T. E. Feuchtwang, A. Notea, and P. H. Cutler, "The Linear Response Theory of the Scanning Tunneling Microscope. I. General Metrological Considerations in the Interpretation of Experimental Data," Surf. Sci. 207, 547 (1989); idem, "The Linear Response Theory of the Scanning Tunneling Microscope. II. Determination of the Phenomenological and Semi-Empirical Instrument Function," ibid. 207, 558 (1989).
- Th. S. Huang, W. F. Schreiber, and O. J. Tretiak, "Image Processing," Proc. IEEE 59, 1586 (1971).
- S. A. Kassam and H. V. Poor, "Robust Techniques for Signal Processing: A Survey," Proc. IEEE 73, 433 (1985).
- G. Binnig, N. Garcia, H. Rohrer, J. M. Soler, and F. Flores, "The Electron-Metal Surface Interaction Potential with Vacuum Tunneling. Observation of the Image Force," *Phys. Rev. B* 30, 4816 (1984).
- P. Muralt and D. W. Pohl, "Scanning Tunneling Potentiometry," Appl. Phys. Lett. 48, 514 (1986).
- B. E. Bayer, "An Optimum Method for Two-Level Rendition of Continuous-Tone Pictures," *IEEE International Conference on Communications, Conference Record*, Cat. No. 73 CHO 744-3CSCB, Paper No. 26-11 (June 1973).
- G. Binnig, H. Rohrer, Ch. Gerber, and E. Stoll, "Real Space Observation of the Reconstruction of Au(100)," Surf. Sci. 144, 321 (1984).
- G. Binnig, H. Rohrer, Ch. Gerber, and E. Weibel, "(111) Facets as the Origin of Reconstructed Au (110) Surfaces," Surf. Sci. 131, L379 (1983).
- A. Selloni, P. Carnevali, E. Tosatti, and C. D. Chen, "Voltage-Dependent Scanning-Tunneling Microscopy of a Crystal Surface: Graphite," *Phys. Rev. B* 31, 2602 (1985).
- 28. I. P. Batra, N. Garcia, H. Rohrer, H. Salemink, E. Stoll, and S. Ciraci, "A Study of Graphite Surface with STM and Electronic Structure Calculations," *Surf. Sci.* 181, 126 (1987).
- J. Tersoff, "Anomalous Corrugations in Scanning Tunneling Microscopy: Imaging of Individual States," *Phys. Rev. Lett.* 57, 440 (1986).
- E. P. Stoll, "Why do 'Dirty' Tips Produce Higher-Resolution Images When Graphite Is Scanned in a Scanning Tunneling Microscope?" J. Phys. C 21, L921 (1988).
- T. Tiedje, J. Varon, H. Deckman, and J. Stokes, "Tip Contamination Effects in Ambient Pressure Scanning Tunneling Microscopy Imaging of Graphite," J. Vac. Sci. Technol. A 6, 372 (1988).
- G. Binnig, Ch. Gerber, E. Stoll, T. R. Albrecht, and C. F. Quate, "Atomic Resolution with Atomic Force Microscope," *Europhys. Lett.* 3, 1281 (1987); *idem*, "Atomic Resolution with Atomic Force Microscope," *Surf. Sci.* 189/190, 1 (1987).
- F. F. Abraham, I. P. Batra, and S. Ciraci, "Effect of Tip Profile on Atomic-Force Microscope Images: A Model Study," *Phys. Rev. Lett.* 60, 1314 (1988); F. F. Abraham and I. P. Batra, "A Theoretical Interpretation of AFM Images of Graphite," *Surf. Sci.* 209, L125 (1989).
- G. Binnig, H. Fuchs, Ch. Gerber, H. Rohrer, E. Stoll, and E. Tosatti, "Energy-Dependent State-Density Corrugation of a Graphite Surface as Seen by Scanning Tunneling Microscope," Europhys. Lett. 1, 31 (1986).
- G. Travaglini, H. Rohrer, M. Amrein, and H. Gross, "Scanning Tunneling Microscopy on Biological Matter," Surf. Sci. 181, 380 (1987)
- G. Travaglini, H. Rohrer, E. Stoll, M. Amrein, A. Stasiak, J. Sogo, and H. Gross, "Scanning Tunneling Microscopy of recA-

- DNA Complexes," Phys. Scripta 38, 309 (1988).
- P. Muralt, H. Meier, D. W. Pohl, and H. W. M. Salemink, "Scanning Tunneling Microscopy and Potentiometry on a Semiconductor Heterojunction," *Appl. Phys. Lett.* 50, 1352 (1987)
- 38. R. J. Hamers, R. M. Tromp, and J. E. Demuth, "Surface Electronic Structure of Si(111)-(7 × 7) Resolved in Real Space," *Phys. Rev. Lett.* **56**, 1972 (1986).

Received November 14, 1989; accepted for publication May 25, 1990

Erich Paul Stoll IBM Research Division, Zurich Research Laboratory, 8803 Rüschlikon, Switzerland. After receiving his degree in physics in 1962 from the Swiss Federal Institute of Technology at Zurich, Dr. Stoll became a research assistant at the Swiss Federal Institute of Reactor Research in Würenlingen. Here he investigated crystal structures with thermal neutrons and the theory of electric and electronic properties of simple metals. In 1968 he received his Dr. sc. nat. degree from the Swiss Federal Institute of Technology in Zurich. After joining the IBM Zurich Research Laboratory in 1970, he worked on computer simulations of phase transitions, critical phenomena, and nonlinear systems until 1982. Since then, Dr. Stoll has contributed to the theory and interpretation of scanning tunneling microscopy. He has developed and implemented the graphics tools used for processing STM and related data on the mainframe computer at his present location. His most recent task has been to assist physicists involved in numerically intensive computing by designing economical algorithms and providing instruction in the efficient use of the IBM 3090 Vector Facility.